inorganics

MDPI

Article

$Mg_2(Co_{1/3}Fe_{1/3}Ni_{1/3})$, $Mg_2(Cu_{1/3}Fe_{1/3}Ni_{1/3})$, $Mg_2(Co_{1/3}Cu_{1/3}Fe_{1/3})$, $Mg_2(Co_{1/3}Cu_{1/3}Ni_{1/3})$, and $Mg_2(Co_{1/4}Cu_{1/4}Fe_{1/4}Ni_{1/4})$ Materials for Hydrogen Storage

Eduardo David Ruiz-Santacruz [1], Paula del Carmen Cintrón Núñez [1,2], Nidia Libia Torres García [1] and Karina Suárez-Alcántara [1,*]

[1] Morelia Unit of Materials Institute Research, National Autonomous University of Mexico, Antigua Carretera a Pátzcuaro No. 8701, Col. Ex Hacienda de San José de la Huerta, Morelia CP 58190, Mexico; 1415036c@umich.mx (E.D.R.-S.); paula.cintron.nunez@cinvestav.mx (P.d.C.C.N.); nidialibia.tg@gmail.com (N.L.T.G.)

[2] Nanoscience and Nanotechnology Program, Centro de Investigación y de Estudios Avanzados (CINVESTAV-IPN), Av. Instituto Politécnico Nacional 2508, San Pedro Zacatenco, Gustavo A. Madero, Ciudad de México CP 07360, Mexico

* Correspondence: karina_suarez@materiales.unam.mx

Abstract: Hydrogen is a promising energy vector; however, its storage in solid-state materials is still an unresolved problem. Hydrogen storage on Mg-based materials is an ongoing research area. Here, five materials, $Mg_2(Co_{1/3}Fe_{1/3}Ni_{1/3})$, $Mg_2(Cu_{1/3}Fe_{1/3}Ni_{1/3})$, $Mg_2(Co_{1/3}Cu_{1/3}Fe_{1/3})$, $Mg_2(Co_{1/3}Cu_{1/3}Ni_{1/3})$, and $Mg_2(Co_{1/4}Cu_{1/4}Fe_{1/4}Ni_{1/4})$, are reported for hydrogen storage. The hydriding and dehydriding reactions in these materials proceed via two steps. The first step is associated with the Mg/MgH_2 equilibrium, while the second step is related to the simultaneous formation of mixtures of hydrided Mg-intermetallics. All of the studied materials demonstrate easy hydriding in mild conditions (15 bar, 300 °C). $Mg_2(Co_{1/3}Fe_{1/3}Ni_{1/3})$ can be considered the best material among the studied series, with a hydrogen storage capacity of 3.8 wt. % and a dehydriding onset temperature of 243 °C. The presence of Cu modified the equilibrium pressure of the second hydriding step and induced partial dehydriding at 250 °C in pressure-composition isothermal testing. The presence of Fe favored the hydrogen uptake in the first hydriding reaction, from 0.5 wt. % at the material without Fe to 1.1–2.2 wt. % in the Fe materials. The elements Co, Co, Cu, and Fe demonstrated synergistic effects on hydriding/dehydriding reactions.

Keywords: hydrogen storage; magnesium intermetallics; multicomponent mixtures; tailoring thermodynamic properties

check for updates

Academic Editors: Andrea Rossin, Chao-Ming Huang and Guan-Ting Pan

Received: 5 March 2025
Revised: 9 April 2025
Accepted: 23 April 2025
Published: 26 April 2025

Citation: Ruiz-Santacruz, E.D.; Núñez, P.d.C.C.; García, N.L.T.; Suárez-Alcántara, K. $Mg_2(Co_{1/3}Fe_{1/3}Ni_{1/3})$, $Mg_2(Cu_{1/3}Fe_{1/3}Ni_{1/3})$, $Mg_2(Co_{1/3}Cu_{1/3}Fe_{1/3})$, $Mg_2(Co_{1/3}Cu_{1/3}Ni_{1/3})$, and $Mg_2(Co_{1/4}Cu_{1/4}Fe_{1/4}Ni_{1/4})$ Materials for Hydrogen Storage. *Inorganics* **2025**, *13*, 135. https://doi.org/10.3390/inorganics13050135

Copyright: © 2025 by the authors. Licensee MDPI, Basel, Switzerland. This article is an open access article distributed under the terms and conditions of the Creative Commons Attribution (CC BY) license (https://creativecommons.org/licenses/by/4.0/).

1. Introduction

Hydrogen storage in solid materials faces many unresolved challenges, such as a high hydrogen storage capacity (6.5 wt. %), storage costs, durability (cyclability), or soft conditions in terms of pressure and temperature in which to operate [1]. These last two conditions are related to hydriding/dehydriding thermodynamics, in the first instance, and kinetics, in the second instance, of the material. MgH_2 faces several challenges; however, for this material, it is mandatory for it to operate at high temperatures due to its high thermodynamic stability. Forming alloys or intermetallics of Mg can be a viable option for hydrogen storage [2]. The potential application areas of Mg intermetallics include industrial and stationary applications [2,3], where hydrogen can be used as a chemical reagent or fuel, and heat would not be an issue in activating the storage/release reactions. For example,

chemical or petrochemical industries use high-purity hydrogen as a reagent and obtain residual heat from unit operations [4]. However, in Mg alloys or intermetallic materials, there is still a need to improve hydriding/dehydriding thermodynamic properties by varying the composition of the materials. In this work, we present multicomponent mixtures of the hydride-forming Mg-intermetallics of Fe, Co, Ni, and Cu, with the aim of tailoring the hydriding/dehydriding thermodynamics while maintaining an adequate hydrogen storage level.

The materials Mg_2FeH_6, Mg_2CoH_5, and Mg_2NiH_4 require lower pressure and temperature conditions for hydriding/dehydriding reactions than pure Mg [2]. Some characteristics of the ternary metal hydrides of Mg ($Mg_2E1_1H_x$, E1 = Fe, Co, or Ni) are as follows: Fe and Mg are not soluble in each other; thus, the mechanical milling or sintering of the elements produces a fine mixture that needs further hydrogen exposition, which, in turn, produces Mg_2FeH_6 with different yields [5–7]. Typically, a lower than expected (5.47 wt. %) quantity of hydrogen content is achieved due to the incomplete reaction. The reactive mechanical milling of MgH_2 and Fe [8], the sintering of Mg and Fe nanoparticles [9], chemical reduction from organometallic precursors [10], or HPT processing [11] are other approaches for the production of Mg_2FeH_6. One reaction from the elements is as follows:

$$2Mg + Fe + 3H_2 \leftrightarrow Mg_2FeH_6, \quad (1)$$

The in situ formation or presence of MgH_2 added as a reactive can play a role in the formation of Mg_2FeH_6 [7,9]:

$$2MgH_2 + Fe + H_2 \leftrightarrow Mg_2FeH_6, \quad (2)$$

Mg_2FeH_6 has a cubic arrangement of a complex octahedral anion $[FeH_6]^{4-}$; the structure is stabilized by Mg^{2+} cations [12,13].

Mg_2CoH_5 (4.48 wt. % hydrogen content) can be produced by: the sintering or mechanical milling of Mg and Co, followed by hydrogen exposition at a high temperature; the milling of MgH_2 and Co, followed by exposition to high hydrogen pressure and temperature; or reactive mechanical milling in a hydrogen atmosphere [14–16]. The relatively easy formation of Mg_2CoH_5, preceded by MgH_2 formation, has been observed below 300 °C and 85 bar [16]. Mg_2CoH_5 has two polymorphs, known as the low- and high-temperature polymorphs (tetragonal and distorted cubic structure, respectively) [15–17]. The low-temperature Mg_2CoH_5 is built up by a square-pyramidal $[CoH_5]^{4-}$ anion complex surrounded by Mg^{2+} cations [16]. The decomposition of Mg_2CoH_5 has been reported, at 300 °C, to produce the elements Mg and Co, as well as some $MgCo_2$ but not Mg_2Co [16]. Mg_2Co did not participate in the Mg-Co phase diagram [18]. The proposed sequence of reactions for Mg_2CoH_5 formation is [16]:

$$2Mg + Co \overset{2H_2}{\rightarrow} 2MgH_2 + Co \overset{0.5H_2}{\rightarrow} Mg_2CoH_5, \quad (3)$$

By itself, Mg_2NiH_4 (3.62 wt. % hydrogen content) is considered a potential alternative for hydrogen storage in a solid material [19–21]. The ball-milling of the elements followed by annealing (400 °C/vacuum) is a well-established method for the synthesis of Mg_2Ni. The formation of Mg_2NiH_4 is accessible by heating in hydrogen or upon the cycling (applying successive hydriding/dehydriding conditions) of the ball-milled elements Mg and Ni. Also, the direct hydriding of precursors is possible in reactive ball-milling [19,22]. The formation reaction is:

$$2Mg + Ni + 2H_2 \leftrightarrow Mg_2NiH_4, \quad (4)$$

The formation of Mg_2NiH_4 from MgH_2 and Ni has also been reported [23]. Mg_2NiH_4 presents at least two polymorphs: the low-temperature and the high-temperature, usually

called LT (monoclinic) and LH (cubic), respectively [24]. In these materials, the tetrahedral anion complex structure, $[NiH_4]^{4-}$, is stabilized by two Mg^{2+} cations [12].

In addition to the hydrides of intermetallic compounds, the Mg-Cu system can be used to destabilize MgH_2 [25]. Mg_2Cu can react reversibly with hydrogen through the formation of MgH_2 [26,27]:

$$2Mg_2Cu + 3H_2 \leftrightarrow 3MgH_2 + MgCu_2 \quad (5)$$

Reaction (5) has been reported to exhibit a lower dehydriding temperature compared to pure MgH_2 [26,28]. Reaction (5) has a theoretical capacity of 2.63 wt. % hydrogen storage, though experimental results have indicated a slightly lower capacity [29]. Both Mg_2Cu and $MgCu_2$ are included in the Mg-Cu phase diagram [28]. Li et al. claimed to produce Mg_2CuH_3 [30], but no clear evidence of that compound was located after a careful literature analysis.

The study of quaternary hydrides of Mg ($Mg_2E1_yE2_zH_x$), with E1 and E2 as Ni, Co, or Fe, was reported a few decades ago. The formation of Mg_2Ni, with the partial substitution of Ni by Co, Fe, or Cu, has been reported with further hydriding reactions [31–33]. Furthermore, $Mg_2Fe_yCo_zH_x$ materials have been reported [34]. The amounts of E1 and E2 (Ni, Co, or Fe) have been somewhat randomly chosen by different researchers in different studies. In general, the metal substitution reduces the decomposition temperature [31–33]. However, the effect of each metal addition to the intermetallics mixture has not been well defined. Moreover, the substitution effects have not been unanimously described in terms of hydriding/dehydriding kinetics or hydrogen uptake. Table 1 summarizes the reported values of reaction pressure and temperature (mostly from pressure-composition isotherms), hydrogen uptake, and the reversibility of the materials commented on in the preceding lines. A direct comparison between published data is difficult because of the great variety of raw materials, synthesis methods, and hydriding/dehydriding conditions. In general, a lower-than-expected hydrogen uptake, a great variability of hydrogen uptake values, and a lack of complete information on the substituted metal hydrides can be observed.

Table 1. Reported values of reaction pressure and temperature, hydrogen uptake, and reversibility of the materials.

Material (Not Hydrided)	Temperature [°C], Pressure [bar]	Hydrogen Storage Capacity [wt. %]	Reversibility and Technique	Number of Equilibrium Plateaus	Raw Materials/Producing Technique/Comments	Reference
Mg_2Fe	300, 100 (20) ≍	4.95	Yes, PCI	1	Nanoparticles from reduction of organometallic precursors	[10]
	350, 100 (5) ≍	5.03	Yes PCI *	1	Sintering of the elements	[9]
	50 to 500, 90–70	4.55	Peaks at 315 °C or 338 °C, DSC	2	Mechanical milling of the elements	[35]
	450–520, 20–120 (32) ≍	4.6	Yes, PCI *	2	Mixed and pressing of elements, hydriding of the pellets for up to 10 days	[12]
	350, 10	5.4	Yes, PCI *	2	Mixing MgH_2 + Fe manually, further 50 hydriding/dehydriding cycles	[5]
	325, 20	4.7	Yes, PCI	1	$2MgH_2$ + Fe, mixing, ball milled and dehydrided	[7]
	***, 75	4.34	Yes, TPD	1	Reactive ball milling of the elements	[14]
$Mg_2Fe + D_2$	RT-500, ***	6.5 **	Yes, TGA *	1	$2MgD_2$ + Fe + D_2, reactive milling at 10 bar D_2 pressure	[8]

Table 1. *Cont.*

Material (Not Hydrided)	Temperature [°C], Pressure [bar]	Hydrogen Storage Capacity [wt. %]	Reversibility and Technique	Number of Equilibrium Plateaus	Raw Materials/Producing Technique/Comments	Reference
Mg_2Co	300, 4.5	1.8	Yes, PCI	2	Mechanical milling of the elements	[36]
	300, 10	1.6	Yes, PCI	2	Reactive mechanical milling of $2MgH_2$ + Co	[37]
	400, 50 (30) ≍	3.0	Yes, PCI	2	Mechanical milling of the elements	[38]
	***, 75	3.80	Yes, TPD	1	Mechanical milling of the elements	[14]
Mg_2Ni	400, 30	3.5	Yes, PCI *	1	Mechanical milling of the elements, then annealing at high temperature	[39]
	250, 10	2.77	Yes, PCI	1	Compressed (pellet) of the elements	[40]
	***, 75	3.03	Yes, TPD	1	Mechanical milling of the elements	[14]
Mg_2Cu	300, 25 (5) ≍	2.6	Yes, PCI	1	Mechanical milling of the elements	[29]
$Mg_2Ni_{0.8}Cu_{0.2}$	300, 40 (25) ≍	3.5	Yes, PCI	2	Melting of the elements. The study covers a range of variations of compositions.	[41]
$Mg_2Ni_{0.75}Fe_{0.25}$	350, 30	2.8	Yes, kinetic (wt. % vs. time)	1	Melting of the elements at 900 °C, pressed into rods, and reheated at 550 °C for several days	[42]
$Mg_2Ni_{0.75}Co_{0.25}$	350, 30	3.1	Yes, kinetic (wt. % vs. time)	1	Melting of the elements at 900 °C, pressed into rods, and reheated at 550 °C for several days.	[42]
$Mg_2Fe_{0.75}Co_{0.25}$	***, 3	3.24	****	1	Reactive ball milling, automatically refilling of H_2 as consumed during milling.	[34]
$Mg_2Fe_{0.5}Co_{0.5}$	***, 50	4.7	****	2	Reactive ball milling	[43]

PCI: Pressure-Composition Isotherm. DSC: Differential scanning calorimetry. TPD: Temperature programmed desorption. TGA: Thermogravimetric analysis. ≍ Pressure values in parentheses correspond to the equilibrium. * Only desorption branch in PCI, usually pre-hydrided in hard conditions of pressure and temperatures. ** Consider D weight twice the H. *** Not estimated/registered during reactive ball milling. **** Not indicated/performed.

The next natural step is developing a systematic survey of quinary hydrides of Mg ($Mg_2E1_wE2_yE3_zH_x$), with E1, E2, and E3 as Ni, Co, Fe, or Cu. In this work, we analyze the kinetics and thermodynamics of hydriding and dehydriding reactions of materials with the following compositions (in alphabetical order of the transition metal): $Mg_2(Co_{1/3}Fe_{1/3}Ni_{1/3})$, $Mg_2(Cu_{1/3}Fe_{1/3}Ni_{1/3})$, $Mg_2(Co_{1/3}Cu_{1/3}Fe_{1/3})$, $Mg_2(Co_{1/3}Cu_{1/3}Ni_{1/3})$, and $Mg_2(Co_{1/4}Cu_{1/4}Fe_{1/4}Ni_{1/4})$. In these materials, the Mg and the sum of the contents of transition metals (Co, Cu, Fe, and Ni) keep a 2:1 atomic ratio. The effects on the kinetics and thermodynamics of each added element are discussed. Paul et al. claim the possibility of adjusting the properties of hydride intermetallics by altering structural and composition characteristics [2]. In this work, we corroborate it.

2. Results

2.1. Hydriding and Dehydriding Reactions

Figure 1a,b presents the third cycle of hydriding and dehydriding reactions of the $Mg_2(Co_{1/3}Fe_{1/3}Ni_{1/3})$, $Mg_2(Cu_{1/3}Fe_{1/3}Ni_{1/3})$, $Mg_2(Co_{1/3}Cu_{1/3}Fe_{1/3})$, $Mg_2(Co_{1/3}Cu_{1/3}Ni_{1/3})$, and $Mg_2(Co_{1/4}Cu_{1/4}Fe_{1/4}Ni_{1/4})$ materials. The hydriding and dehydriding reactions (kinetics) were performed by means of consecutive temperature-programmed hydriding (TPH) and temperature-programmed dehydriding (TPD) experiments. The materials were considered fully activated by the third cycle of hydriding and dehydriding reactions. The

first to third cycles for each material are available in Figures S1, S7, S13, S19, and S25 in the Supplementary File. It must be noted that because of the large number of experiments, data, and images, many of the commented-on results are presented in the Supplementary File (there are 36 slides presenting the results). Readers are invited to check the Supplementary File for detailed images and data.

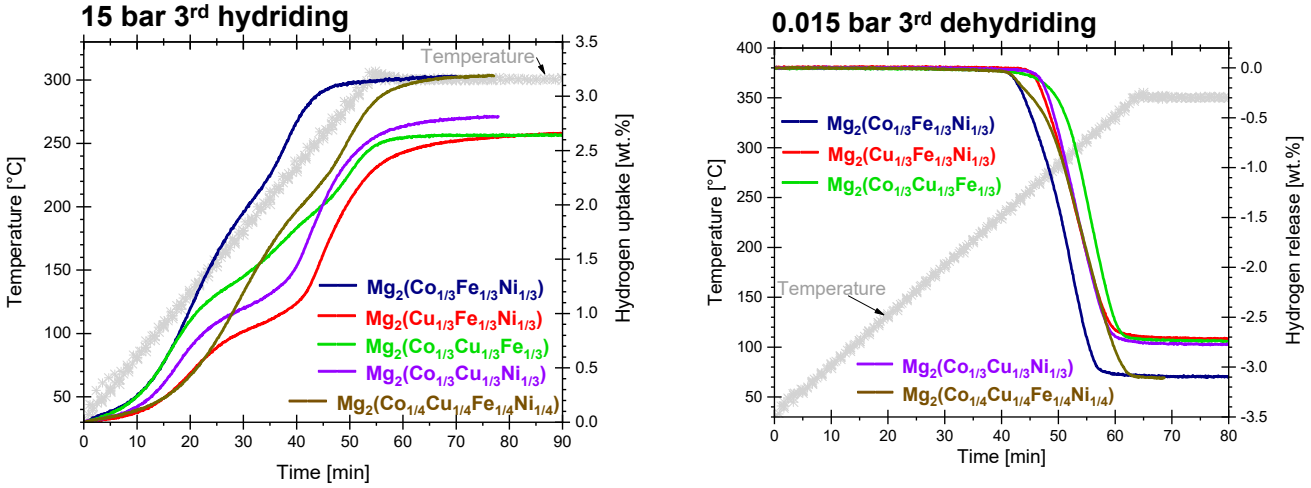

(**a**) (**b**)

Figure 1. (**a**) Hydriding and (**b**) dehydriding third cycle for $Mg_2(Co_{1/3}Fe_{1/3}Ni_{1/3})$, $Mg_2(Cu_{1/3}Fe_{1/3}Ni_{1/3})$, $Mg_2(Co_{1/3}Cu_{1/3}Fe_{1/3})$, $Mg_2(Co_{1/3}Cu_{1/3}Ni_{1/3})$, and $Mg_2(Co_{1/4}Cu_{1/4}Fe_{1/4}Ni_{1/4})$ materials.

From the first to the third cycles, an increase in hydrogen uptake and kinetics was confirmed (Tables S1–S5 in the Supplementary File). Roughly, an increase between 0.1–0.3 wt. % was observed for the maximum hydrogen uptake, and a reduction of the onset hydriding temperature of about 100 °C was obtained. For the dehydriding reactions, the $Mg_2(Co_{1/3}Cu_{1/3}Fe_{1/3})$ and $Mg_2(Co_{1/3}Fe_{1/3}Ni_{1/3})$ presented a reduction of the onset temperature of about 30 °C and 60 °C, respectively, upon cycling. The rest of the materials presented a decrease between 0 and 10 °C, i.e., a really minor change. As stated in the experimental section, the threshold to define the beginning of the hydriding and dehydriding reactions was chosen as the uptake or release of 0.1 wt. % hydrogen, respectively.

In general, the materials demonstrated lower-than-expected hydrogen storage capacities, as shown in Figure 1a. The expected and observed hydrogen content is summarized in Table 2. The expected values were estimated considering the complete formation of the hydrides according to Equations (1), (3)–(5), and the stoichiometry of the metals in the initial mixture. The material with the higher hydrogen storage expectancy was $Mg_2(Co_{1/3}Fe_{1/3}Ni_{1/3})$, which experimentally resulted in a hydrogen storage value of 3.18 wt. % at 15 bar and 300 °C. For its part, the $Mg_2(Co_{1/4}Cu_{1/4}Fe_{1/4}Ni_{1/4})$ stored a value of 3.19 wt. % hydrogen. The remaining materials stored between 2.6 and 2.8 wt. % of hydrogen under the same conditions. An important point to notice is that the hydriding conditions of pressure and temperature could be considered mild; better hydrogen storage values might be obtained with higher hydrogen pressures. The mild pressure conditions were selected intentionally to prove easy hydriding reactions. Another important point to notice is the low onset hydriding temperature and relatively high hydriding kinetics. The hydriding onset temperature is 55 °C for the $Mg_2(Co_{1/3}Fe_{1/3}Ni_{1/3})$ material. The same material, $Mg_2(Co_{1/3}Fe_{1/3}Ni_{1/3})$, reached 80% of the experimental capacity at 220 °C. As observed in Figure 1a, the hydriding reactions at the studied materials are a multistep process; two hydriding steps can be associated with the changes in slope in the hydriding curves.

Table 2. Third hydriding and dehydriding reaction data for $Mg_2(Co_{1/3}Fe_{1/3}Ni_{1/3})$, $Mg_2(Cu_{1/3}Fe_{1/3}Ni_{1/3})$, $Mg_2(Co_{1/3}Cu_{1/3}Fe_{1/3})$, $Mg_2(Co_{1/3}Cu_{1/3}Ni_{1/3})$, and $Mg_2(Co_{1/4}Cu_{1/4}Fe_{1/4}Ni_{1/4})$ materials.

Material	Maximum Expected Hydrogen Storage [wt. %]	Hydrogen Uptake at 15 bar and 300 °C	Onset Hydriding Temperature at 15 bar, +0.1 wt. % [°C]	Temperature Reaching 80% Hydrogen Storage [°C]	Onset Dehydriding Temperature at 0.015 bar, −0.1 wt. % [°C]	Hydrogen Uptake in PCI Experiments [wt. %]	Equilibrium Pressure at 300 °C, First and Second Hydriding Plateaus [bar]
$Mg_2(Co_{1/3}Fe_{1/3}Ni_{1/3})$	4.48	3.18	55	220	243	3.80	0.55, 2.29
$Mg_2(Cu_{1/3}Fe_{1/3}Ni_{1/3})$	3.55	2.66	87	293	263	3.43	0.68, 6.02
$Mg_2(Co_{1/3}Cu_{1/3}Fe_{1/3})$	3.78	2.64	58	265	262	3.17	0.52, 4.62
$Mg_2(Co_{1/3}Cu_{1/3}Ni_{1/3})$	3.57	2.81	72	268	264	3.06	0.65, 5.92
$Mg_2(Co_{1/4}Cu_{1/4}Fe_{1/4}Ni_{1/4})$	3.75	3.19	77	279	245	3.51	0.53, 6.07

The dehydriding reactions, as shown in Figure 1b, indicate that the materials presented good reversibility, releasing all the stored hydrogen with a minor loosening of capacity over the first three cycles. The lowest onset for the dehydriding reaction was observed for the $Mg_2(Co_{1/3}Fe_{1/3}Ni_{1/3})$ material at 243 °C. Meanwhile, the maximum hydrogen release rate occurred at 292 °C for the $Mg_2(Co_{1/3}Fe_{1/3}Ni_{1/3})$ and a few Celsius degrees higher for the rest of the materials (Supplementary File, Figure S31; first derivative of dehydriding reactions). Remarkably, the dehydriding reactions were performed in a single step under the conditions presented in Figure 1b, except for $Mg_2(Co_{1/4}Cu_{1/4}Fe_{1/4}Ni_{1/4})$. A possible explanation for this behavior is that as soon as the hydrided intermetallics decompose to MgH_2, this material releases the remaining hydrogen at such low pressures, without producing slope changes at the TPD curves.

Figure 2a presents the pressure composition isotherm (PCI) charts for the hydriding/dehydriding of the five materials at 300 °C. The PCI charts for different temperatures (250–350 °C) can be observed in Figures S1, S7, S13, S19, and S25 of the Supplementary File. Figure 2a presents the multi-step nature of the hydriding and dehydriding reactions. Two plateaus can be observed in all materials; hereafter, we identify them as the low-pressure and high-pressure plateaus, respectively. The low-pressure plateaus can be associated with the formation of MgH_2, while the second set of plateaus can be associated with the formation of the hydrided intermetallics of Mg. The red dotted line in Figure 2a at 0.718 bar indicates the expected Mg/MgH_2 equilibrium pressure at 300 °C, calculated with the Van't Hoff equation [44]:

$$ln\left(\frac{P_{eq}}{P_{eq}^0}\right) = \frac{\Delta H}{RT} - \frac{\Delta S}{R}, \quad (6)$$

where the equilibrium pressure, p_{eq}, is related to the changes ΔH and ΔS, enthalpy and entropy, respectively [44]. The entropy change corresponds mainly to the change from molecular hydrogen gas to hydrogen atoms forming part of an ordered solid [44]; it is frequently taken as $\Delta S = -130$ J·K^{-1} mol^{-1} H_2 [44]. T and R have their usual meaning. The experimental values of the hydriding equilibrium pressures at 300 °C are collected in Table 2. It must be noted that the low-pressure plateaus are shifted slightly below the thermodynamic value of 0.718 bar for the Mg/MgH_2 equilibrium at 300 °C. This indicates the easiness of the first hydriding reaction and some difficulty of the dehydriding reaction, especially at temperatures lower than 300 °C (Figures S1, S7, S13, S19, and S25 of the Supplementary File).

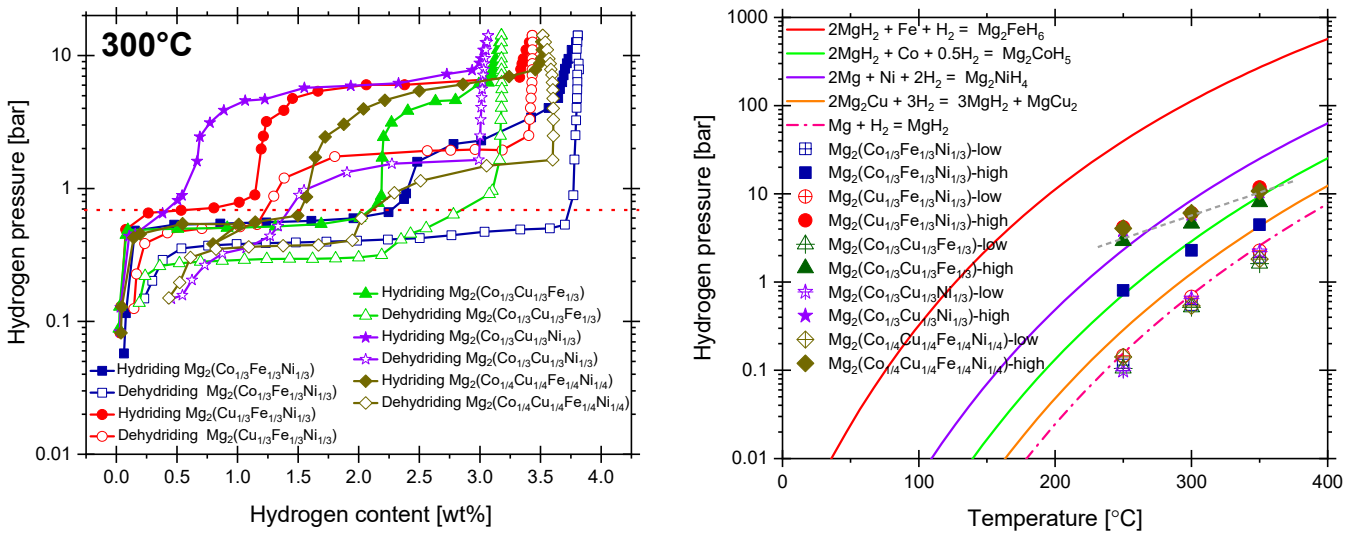

(**a**) (**b**)

Figure 2. (**a**) PCI curves of $Mg_2(Co_{1/3}Fe_{1/3}Ni_{1/3})$, $Mg_2(Cu_{1/3}Fe_{1/3}Ni_{1/3})$, $Mg_2(Co_{1/3}Cu_{1/3}Fe_{1/3})$, $Mg_2(Co_{1/3}Cu_{1/3}Ni_{1/3})$, and $Mg_2(Co_{1/4}Cu_{1/4}Fe_{1/4}Ni_{1/4})$ materials at 300 °C. (**b**) Calculated equilibrium pressures of the reactions (2), (3), (4), and (5) for the formation of Mg-intermetallics and Mg/MgH_2. The dots indicated the observed equilibrium pressures for the studied materials.

Meanwhile, the second plateau was displaced to higher pressures than the equilibrium pressure of Mg/MgH_2. The material that presented the lowest shift to higher pressures was $Mg_2(Co_{1/3}Fe_{1/3}Ni_{1/3})$, reaching equilibrium at 2.29 bar. The rest of the materials presented higher equilibrium pressures (4.62–6.07 bar); all of them have in common the presence of Cu. Ideally, the shift to higher equilibrium pressure must benefit the dehydriding reaction and reversibility. This is because, at a given temperature, extremely low pressure or even vacuum conditions would be required to complete dehydriding if the material presents a low equilibrium pressure. Conversely, high equilibrium pressures indicate the need for moderate temperatures to perform dehydriding. Because of that, the materials $Mg_2(Cu_{1/3}Fe_{1/3}Ni_{1/3})$, $Mg_2(Co_{1/3}Cu_{1/3}Fe_{1/3})$, $Mg_2(Co_{1/3}Cu_{1/3}Ni_{1/3})$, and $Mg_2(Co_{1/4}Cu_{1/4}Fe_{1/4}Ni_{1/4})$ demonstrated partial dehydriding at 250 °C (PCI curves in Figures S7, S13, S19, and S25 of the Supplementary File). Additionally, the extension (longitude) of the plateaus varied among the different materials. For the $Mg_2(Co_{1/3}Fe_{1/3}Ni_{1/3})$, the low-pressure plateau extends up to 2.25 wt. %. Meanwhile, for the $Mg_2(Co_{1/3}Cu_{1/3}Ni_{1/3})$ material, the low-pressure plateau extends only to about 0.50 wt. %. In increased order of the extension of the first plateau for the rest of the materials, they were: $Mg_2(Cu_{1/3}Fe_{1/3}Ni_{1/3})$ with 1.14 wt. %, $Mg_2(Co_{1/4}Cu_{1/4}Fe_{1/4}Ni_{1/})$ with 1.5 wt. %, and $Mg_2(Co_{1/3}Cu_{1/3}Fe_{1/3})$ with 2.16 wt. %. The presence of Fe seems to improve the hydrogen uptake in the first equilibrium. In turn, the hydrogen uptake at the low-equilibrium pressure seems to have had a consequential effect on the total hydrogen uptake because the material ($Mg_2(Co_{1/3}Cu_{1/3}Ni_{1/3})$) with the lower hydrogen uptake in the first reaction also presented the lower final hydrogen uptake in PCI experiments, i.e., 3.06 wt. %. Conversely, the material with the higher hydrogen uptake in the first reaction also presented the best total hydrogen uptake, $Mg_2(Co_{1/3}Fe_{1/3}Ni_{1/3})$, with 3.80 wt. %.

The PCI curves confirm that $Mg_2(Co_{1/3}Fe_{1/3}Ni_{1/3})$ is the most effective hydrogen storage material among the materials reported here because of the hydrogen storage value of 3.8 wt. % (Table 2). The hydrogen storage values of the PCI curves are higher than the results obtained in the temperature-programmed hydriding and dehydriding reactions. This effect is due to the long experiment duration (5–7 days per PCI curve), i.e., between

0.5 and 4 h per point as compared to 1.5 h at the kinetic experiments. As PCI experiments are related to thermodynamic data, the longer the experiments, the better the results. Finally, all of the studied materials presented a significant degree of hysteresis between the hydriding and dehydriding branches of the PCI curves, in particular for the high-pressure plateaus. This indicated a great degree of complexity in the dehydriding reactions, strong dependence on pressure, and changes compared to the hydriding reactions of the composite intermetallics. The underlying reason for this is the formation and decomposition of the hydrided intermetallics and destabilization of $Mg_2Cu/MgCu_2$, as it involves great changes in the structures of the materials.

Figure 2b presents the calculated pressure-temperature equilibrium lines for the different hydrided intermetallics of Mg mentioned in the introduction section. These hydrided intermetallics can be part of the composite materials upon the hydriding of the ball-milled materials. The Van't Hoff expression (Equation (6)) was used for obtaining the equilibrium lines [44]. The enthalpy values were used as follows: The MgH_2 was included as the reference material, and its formation enthalpy was used as −76.15 kJ/mol H_2 [45]. The formation of Mg_2NiH_4 was included because of the easiness of the direct reaction from the elements; the formation enthalpy was −64.4 kJ/mol H_2 [46]. Figure 2b also presents the pressure-temperature equilibrium lines of reactions (2), (3), and (5), i.e., the reactions of the transition metals Fe, Co, and Cu with MgH_2 in a hydrogen atmosphere. A reaction enthalpy (theoretical) of −52.06 kJ/mol H_2 [47] was used for the reaction (2). Meanwhile, a value of −69.5 kJ/mol H_2 (experimental) was used for the second part of the reaction (3) [37]. For the reaction (5), a value of −73.51 kJ/mol H_2 was calculated using classic thermodynamics calculations from the formation enthalpy of Mg_2Cu (−9.6 kJ/mol) [48], $MgCu_2$ (−11.3 kJ/mol) [48], and MgH_2 [45].

The red equilibrium line for reaction (2), Mg_2FeH_6 production, presents the highest increase in equilibrium pressure compared to the Mg/MgH_2 equilibrium (pink dotted line). In contrast, the orange equilibrium line for the Cu-containing material (reaction (5)) presents the smallest shift to higher equilibrium pressures. The dots in Figure 2b present the hydriding equilibrium pressures of the tested materials (listed in Table 2, extracted from PCI data; Figures S1, S7, S13, S19, and S25 of the Supplementary File). The crossed dots represent the low-equilibrium pressures, while the filled dots represent the high-equilibrium pressures. In general, the low-pressure equilibrium points closely followed the calculated equilibrium pressure of Mg/MgH_2. However, as mentioned before, the equilibrium is slightly lower than the pure Mg/MgH_2 system. For the high-pressure equilibrium points, the behavior did not follow any of the equilibrium lines of the reactions for producing hydrided Mg-intermetallics or destabilization by $Mg_2Cu/MgCu_2$. The $Mg_2(Co_{1/3}Fe_{1/3}Ni_{1/3})$ presented the smallest pressure shift. Meanwhile, the rest of the materials are closely grouped (grey dotted line). From the PCI curves, it can be confirmed that adding Cu increased the equilibrium pressure of the second hydriding reaction.

2.2. Characterization of the As-Milled and Hydrided Materials

The XRD patterns of the as-milled materials are presented in Figure 3a. The samples presented a progressively increased background signal that can be related to the fluorescence effects of the metals present in the samples. All of the diffractograms present the peak of the Kapton film used for protection against unwanted oxidation. The Kapton peak is located between 10° and 30° in 2θ (2theta) and is useful for comparing the relative intensities of the rest of the peaks. In that regard, the as-milled materials importantly reduced their crystal size after the intensive milling process. The as-milled materials present the main peaks of Mg and a prominent and relatively broad peak located around 44.6° that collects the main peaks of Fe (BBC (110)), Ni (FCC (111)), and a peak of hexagonal Co (002). The

peaks signaled in red correspond to the most intense expected peaks of the Co, Cu, Fe, or Ni metals. For the case of Co, the expected main peak is located at 47.4° in 2θ for hexagonal Co. The relatively low intensity of the Co peaks indicates a good integration or amorphization of this element in particular. In contrast, the relatively high intensity of Fe and Cu peaks indicates a reduced integration or amorphization of these metals in the Mg matrix, which is expected for Fe but not for Cu. No evidence of crystalline Mg-intermetallics was registered after milling.

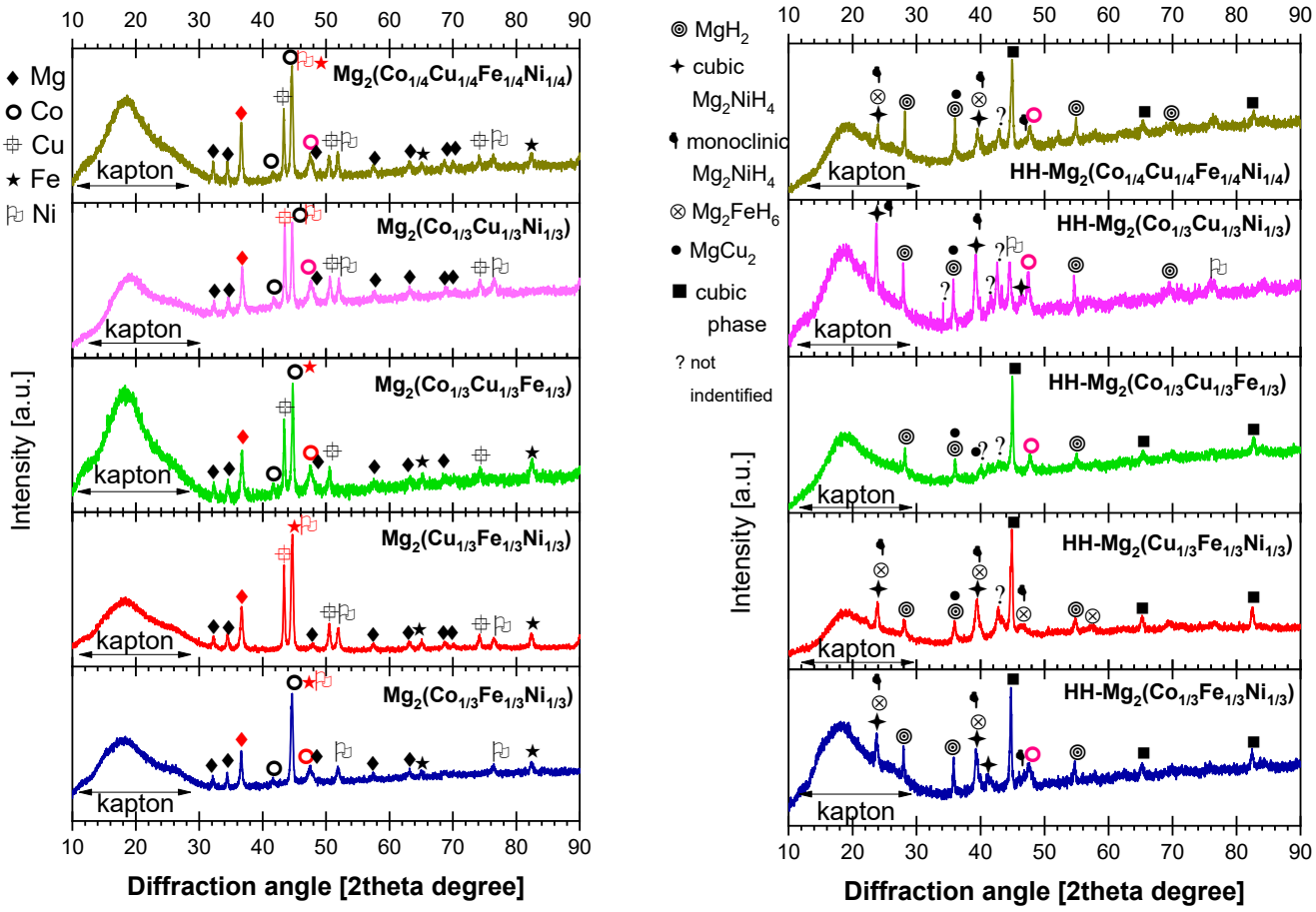

(**a**) (**b**)

Figure 3. X-ray diffraction of the (**a**) as-milled and (**b**) hydrided (HH-) materials. The reference materials used were: Mg ICSD-642654, Co COD-9008492, Cu COD-9008468, Fe COD-9008536, Ni COD-9008476, MgH_2-ICDS 161962, $MgCu_2$ COD-1563768, cubic-Mg_2NiH_4 COD-1521145, and monoclinic-Mg_2NiH_4 COD-1524991, and the Mg_2CoH_5 crystal structure was constructed from data in [16]. The Mg_2FeH_6 crystal structure was constructed from data in [12,13].

Figure 3b presents the X-ray diffraction (XRD) patterns taken after hydriding at 300 °C and 15 bar; the materials are not fully hydrided, according to the theoretical values and Figures 1 and 2. In general, the materials present the characteristic peaks of MgH_2, but their relative intensity does not surpass the peak intensity of the Kapton. No indications of residual Mg can be observed. Another important observation is that the most prominent peak in the XRD pattern of hydrided materials corresponds to a cubic phase. The intensity of that peak is reduced compared to the as-milled materials, and their position is displaced slightly to higher diffraction angles of Fe, except for $Mg_2(Co_{1/3}Cu_{1/3}Ni_{1/3})$ (Figures S2, S8, S14, S20, and S26 of the Supplementary File). Thus, the cubic-identified peak is the remaining (unreacted) Fe content in the sample but might partially dissolve other metals during the successive heating and cooling of hydriding/dehydriding cycling.

The formation of the hydrided intermetallic (cubic) Mg_2FeH_6 is indicated by the presence of its peaks in $Mg_2(Co_{1/3}Fe_{1/3}Ni_{1/3})$, $Mg_2(Cu_{1/3}Fe_{1/3}Ni_{1/3})$, and $Mg_2(Co_{1/4}Cu_{1/4}Fe_{1/4}Ni_{1/4})$. However, the (cubic) Mg_2FeH_6 diffraction peaks are very close to the peaks produced by the high-temperature (cubic) polymorph of Mg_2NiH_4. Additionally, the low-temperature (monoclinic) phase of Mg_2NiH_4 produces a widening of the peaks at about 23.70° and 39.16° because several peaks of this phase are located around these diffraction angles. This means cubic and monoclinic peaks of Mg_2NiH_4 and cubic Mg_2FeH_6 peaks are collected in the broad peaks at about 24° and 39° in 2θ. Another interesting characteristic is that the Mg_2FeH_6 and Mg_2NiH_4 peaks are absent in the material without Ni, the $Mg_2(Co_{1/3}Cu_{1/3}Fe_{1/3})$. In this material, the absence of Mg_2NiH_4 peaks is obvious, but the presence of cubic Mg_2FeH_6 would be expected. This suggests that the peaks labeled both as cubic Mg_2FeH_6 and cubic/monoclinic Mg_2NiH_4 have a strong component of Mg_2NiH_4, or the cubic Mg_2FeH_6 and cubic/monoclinic Mg_2NiH_4 are synergistically formed when Ni is present.

For the materials that contain Co, a remnant of the most intense metallic Co peak can be observed. Additionally, in some of the Co materials, $Mg_2(Co_{1/3}Cu_{1/3}Fe_{1/3})$, $Mg_2(Co_{1/3}Cu_{1/3}Ni_{1/3})$, and $Mg_2(Co_{1/4}Cu_{1/4}Fe_{1/4}Ni_{1/4})$, an unknown set of peaks emerged between 40 and 42°. These peaks are close to some of the low-temperature peaks of the Mg_2CoH_5 (the main peak is located at 40.39° and a minor peak at 42.74°). However, a perfect match was not obtained. The unknown peaks can also be related to intermetallic phases of the metals in addition to Mg-intermetallics.

Interestingly, the peaks of metallic Cu disappeared after hydriding; the expected formation of $MgCu_2$ was not confirmed because the main peak (100% relative intensity) of $MgCu_2$ is located at 28.0°, which is located at the zone of the Kapton peak. The next intense peak (94.18% relative intensity) of $MgCu_2$ is located at 35.83°, coinciding with the (101) peak of MgH_2.

The last characteristic to comment on is the low intensity of the peaks. This led us to conclude that significant fractions of the hydrided products are in an amorphous state. Even for the hydrided materials, the XRD indicated that the number of hydriding/dehydriding cycles is not enough to produce changes in the amorphous nature of materials. The XRD characterization reveals a high degree of complexity in the crystalline and amorphous phases of the hydrided materials.

In this work, the $Mg_2(Co_{1/3}Fe_{1/3}Ni_{1/3})$ demonstrated a good balance between hydrogen storage capacity and kinetics. Figure 4 presents the scanning electron microscopy (SEM) image and the elemental mapping of the as-milled $Mg_2(Co_{1/3}Fe_{1/3}Ni_{1/3})$ chosen as a representative material. Figure 4a presents the SEM micrograph of the as-milled $Mg_2(Co_{1/3}Fe_{1/3}Ni_{1/3})$. The material comprises semi-spherical agglomerates of sizes between 10 and 250 μm. Despite the long milling time and the high-energy milling, the as-milled materials still present a segregation of the elements Co, Fe, and Ni in the Mg matrix (Figure 4b). The elemental contrast reveals significant bright areas of these elements, but there is a predominant presence of Fe in irregular areas of about 10 μm × 10 μm. For the rest of the materials, the SEM micrographs (Figures S3, S9, S15, S21, and S27) and elemental mappings (Figures S4, S10, S16, S22, and S28) of as-milled materials can be consulted in the Supplementary File at different magnifications and detectors. In general, among the added elements, Fe is the metal least integrated into the as-milled materials, followed by Co. By comparison, Ni and Cu showed better integration into the Mg matrix in the elemental mappings (Figures S4, S10, S16, S22, and S28). Overall, the materials are non-porous, fused balls of transition metals, and the Mg keeps them together.

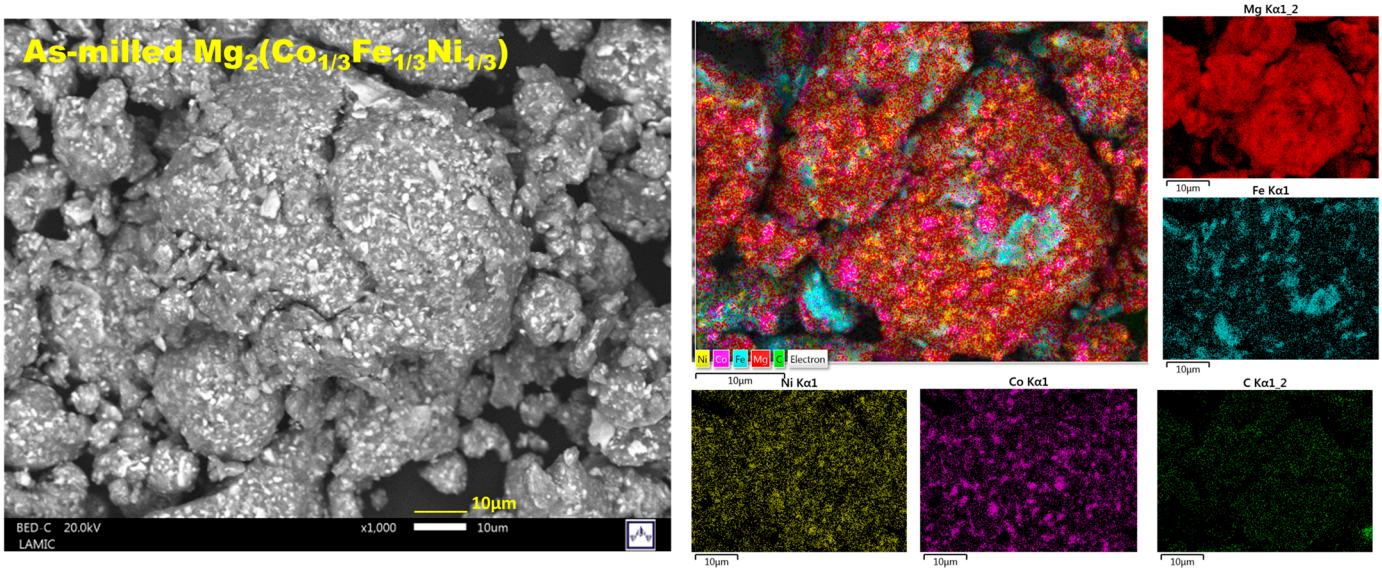

(**a**) (**b**)

Figure 4. (**a**) SEM micrographs and (**b**) elemental mapping of as-milled $Mg_2(Co_{1/3}Fe_{1/3}Ni_{1/3})$.

Figure 5 presents the SEM micrograph and the elemental mapping of the hydrided $Mg_2(Co_{1/3}Fe_{1/3}Ni_{1/3})$ material. For the rest of the hydrided materials, SEM micrographs (Figures S5, S11, S17, S23, and S29) and elemental mappings (Figures S6, S12, S18, S24, and S30) can be consulted in the Supplementary File at different magnifications and detectors. Figure 5 reveals the improved integration of Co and Ni into the Mg matrix. For Fe, the size of the Fe-rich zones reduced in size to less than 5 µm × 5 µm areas. Interestingly, in the hydrided series of micrographs, the elemental contrast is less evident. The whole set of SEM images suggests that the diffusion of Cu, Co, Ni, and Fe occurs during the cycles associated with hydriding and dehydriding processes. However, the Fe integration is less effective than the other metals.

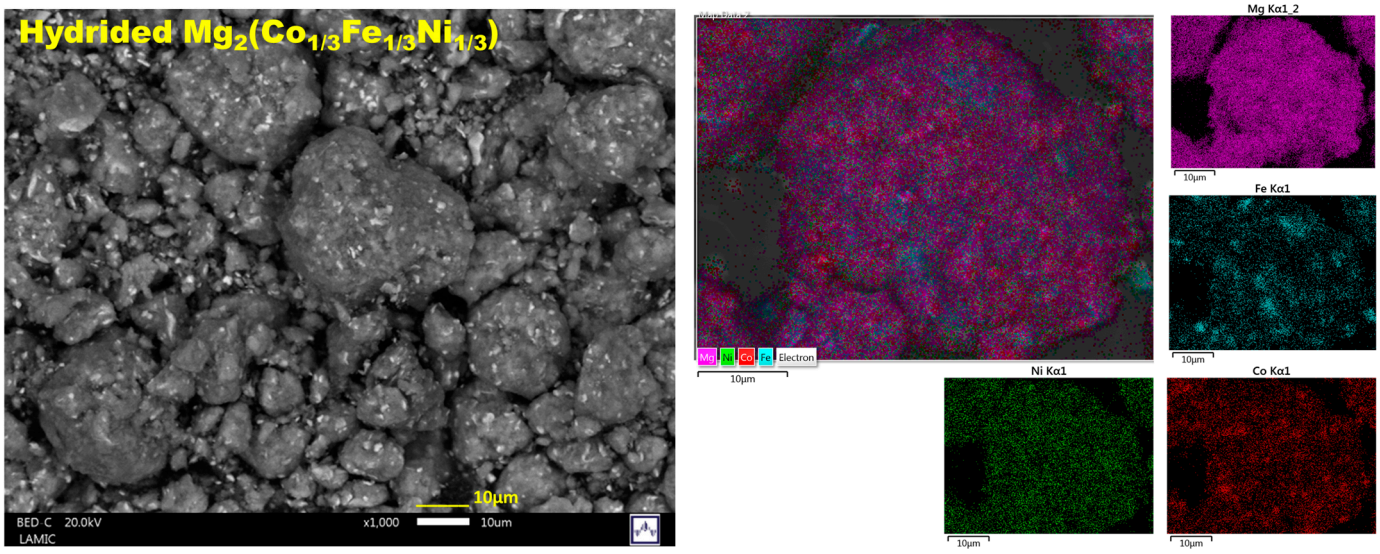

(**a**) (**b**)

Figure 5. (**a**) SEM micrographs and (**b**) elemental mapping of hydrided $Mg_2(Co_{1/3}Fe_{1/3}Ni_{1/3})$.

3. Discussion

Under the correct milling conditions (with long milling times and high energy), the possible intermetallics of Mg with Ni and Cu are, respectively, Mg_2Ni and $MgNi_2$, and Mg_2Cu and $MgCu_2$ [49]. Additionally, the Mg-Cu system has a certain degree of intermiscibility among its phases [28]. Meanwhile, the solubility of Mg-Fe is highly limited [6,50], and the Mg-Co phase diagram does not include Mg_2Co but $MgCo_2$ [18]. However, as observed in the XRD and SEM results, and despite the high energy of milling, the mechanical milling produced mixtures of the elements Mg without the formation of intermetallics. The mixtures have significant areas of segregated Fe and Co.

The formation of Mg_2FeH_6 and Mg_2CoH_5 has been reported to be related to a two-step process [7,9,15] where the hydriding of Mg is recognized as the first step. The formation of MgH_2 is frequently associated with an excess of Mg in Mg-Fe or Mg-Co mixtures [14]. Meanwhile, the Mg_2NiH_4 formation presents only one plateau in PCI tests when started from the elements [51]. The reaction of Mg_2Cu with hydrogen is reported to have two plateaus when an excess of Mg is present [26]. In that work, the plateau at lower pressure is identified as the formation of MgH_2, while the second plateau probably refers to the reaction (5) [26]. Consequently, reaction (5) presented a lower dehydriding temperature than pure MgH_2 [26,28]. This effect was explained as a catalytic action of Mg_2Cu over MgH_2 [26], but reaction (5) is more of a destabilization-type effect of MgH_2 [25]. However, in a study on the hydriding of $Mg_2(Cu_{1-x}Ni_x)$, x = 0–1, the PCI curves demonstrated changes in the equilibrium pressures (increased versus Mg_2Ni alone), while the hydrogen uptake was increased with the lower Cu content [41].

In this work, the presence of several metals forming different hydrided Mg-intermetallics prompted us to expect the presence of several hydriding/dehydriding steps at different equilibrium pressures [32,52]. However, as observed in Figures 1 and 2, the hydriding/dehydriding reactions of the studied materials have only two steps (two equilibrium pressures). All of the presented information indicates that, in the studied materials, MgH_2 is formed in the first step, followed by the simultaneous formation of hydrided intermetallics of Mg with Co, Fe, or Ni. The second reaction equilibrium does not follow any pressure-temperature equilibrium lines for producing individual hydrided Mg-intermetallics or destabilization by $Mg_2Cu/MgCu_2$. Cu does not form an intermetallic compound but plays an important role in modifying the equilibrium pressures of the formation of hydrided intermetallics of Mg. Shifting to higher equilibrium pressures is beneficial for dehydriding reactions. However, Cu reduces the hydrogen uptake because of a lack of hydrided Mg-Cu intermetallic.

The presence of only one equilibrium pressure for the collective formation of the hydrided Mg-intermetallics indicates a synergic effect of the elements Co, Cu, Fe, and Ni present in the studied materials. Elements such as Fe, Ni, or Co, or high entropy alloys (HEAs) containing those elements, can catalyze the MgH_2 dehydriding [53,54]. In a recent paper, a Cu-Ni-Co-Fe multicomponent alloy was used to catalyze hydriding/dehydriding reactions on Mg/MgH_2 [55]. In the present work, Fe, Ni, or Co can have a catalytic effect, in addition to the mentioned synergic impact, on the hydriding and dehydriding properties of Mg. The catalytic effect operates in the first step for the formation of MgH_2, and then a synergistic effect in the second step for the formation of mixed intermetallics. Among Fe, Ni, and Co, the principal catalytic effects can be due to Fe. This claim is justified due to the high quantity of stored hydrogen in materials with Fe. Adding Fe increases the extension of the first hydriding plateau, increasing the total hydrogen uptake, as observed in the PCI curves in Figure 2a. However, less integration of Fe in the Mg matrix and an incomplete reaction of Fe to form Mg_2FeH_6 were observed. Adding Ni also has catalytic effects, reducing the hydriding and dehydriding onset temperatures (as observed in Figure 1a and PCI curves

at 250 °C in the Supplementary File). Adding Co improves the hydrogen uptake at a given temperature, as observed in Figure 1a. Thus, further experiments on Mg-Co-Cu-Fe-Ni materials can be performed by adjusting (optimizing) the transition metal content according to their effects.

Comparing the results presented in Table 2 and Figures 1 and 2 with the other published data summarized in Table 1, our multi-component mixtures of the intermetallics of Mg for hydrogen storage presented similar hydrogen uptake to the well-known Mg_2NiH_4, but softer conditions of pressure and temperature were employed. Also, improvements in the reversibility (hydrogen release at 250 °C; Supplementary File figures) were observed. The equilibrium pressures were modified, opening up the possibility of an effective tailoring of properties according to the presence of certain metals and their proportions.

Diffusion is a key factor in hydrogen storage in solid materials; hydriding/dehydriding involves the diffusion of hydrogen atoms and the phase boundary transformation between the hydrided and the dehydrided phases. The recognized element that diffuses in the Mg-based materials is H; however, SEM images and elemental mapping of as-milled versus hydrided materials indicated the diffusion and integration of Cu, Ni, and Co elements in the Mg matrix. For Cu, the dissolution of this metal, presumably for Mg, can be the reason for the lack of its diffraction peaks at the hydrided materials. The integration of Ni and Co is partial. The integration of Fe into Mg is not expected because of the low solubility of the elements; still, a certain degree of the integration of Fe into the mixture of materials is evidenced in the SEM images. Zhang et al., based on CALPHAD results, indicated that, even in a material such as a high entropy alloy, which has been attributed as having a sluggish diffusion and slow phase transformation kinetics, atom diffusion can occur [56]. In the presented materials, the repeated heating and cooling in a hydrogen/vacuum atmosphere during hydriding/dehydriding cycling reduced the size of domains of the Ni, Co, Fe, and Cu elements. The intermixing of all the added elements seems to be beneficial for hydrogen storage.

4. Materials and Methods

4.1. Mixtures Preparation

All raw materials were used as received; they were Mg, Co, Cu, Fe, and Ni powders (all Alfa-Aesar, −325 mesh, 99.86% purity). The stoichiometric quantities to produce 2 g per batch of $Mg_2(Co_{1/3}Fe_{1/3}Ni_{1/3})$, $Mg_2(Cu_{1/3}Fe_{1/3}Ni_{1/3})$, $Mg_2(Co_{1/3}Cu_{1/3}Fe_{1/3})$, $Mg_2(Co_{1/3}Cu_{1/3}Ni_{1/3})$, and $Mg_2(Co_{1/4}Cu_{1/4}Fe_{1/4}Ni_{1/4})$ were confined with six yttria-stabilized zirconia balls of 1 cm in diameter in a stainless-steel milling vial of 50 mL volume. The ball-to-powder ratio was 10:1. All of the storage, handling, and preparation of materials were conducted under an argon atmosphere in a Vigor® glove box (with O_2 and H_2O levels below 5 ppm). Closing of the milling vial, which contained the metal powders and balls, was performed in an argon atmosphere. Then, the milling vial was transferred to a shaker-type mill (cryogenic Retsch®). The cryogenic mill of Retsch® allows milling at cryogenic (liquid N_2) or room temperature conditions and programming cycles of milling/pauses with agitation rates between 5 and 40 Hz [45]. The millings were performed without cooling at a 30 Hz agitation rate, which is considered a high-energy milling. The total milling time was 20 h, and it was divided into 40 cycles of 30 min milling and 10 min pause.

4.2. Hydriding and Dehydriding Reactions

Temperature-programmed hydriding (TPH) and temperature-programmed dehydriding (TPD) experiments were carried out in a Sieverts-type apparatus of our design and construction [57]. The apparatus combines the features of twin lines (sample and refer-

ence) to eliminate thermal effects on the reservoir and sample-holder volumes with a Δp approach [57]:

$$\Delta p = \Delta p_{sample} - \Delta p_{reference} \quad (7)$$

In the manometric apparatus, the measurements of H_2 pressure and temperature, along with the knowledge of the void volumes, an appropriate equation state for H_2 (Hemmes state equation for Z_{fact} calculation), and a mass balance translate into hydrogen uptake/release in wt. %:

$$wt\% = 100 * \frac{MH_2 * \Delta p * V_{sample}}{m * R * T_{sample} * Z_{fact}} + 100 * \frac{MH_2 * \Delta p * V_{reservoir}}{m * R * T_{reservoir} * Z_{fact}} \quad (8)$$

where MH_2 is the hydrogen molar mass (2.01588 g mol^{-1}). Δp is defined in Equation (7). This Δp performs as a differential pressure transducer and helps reduce small variations of the pressures caused by thermal effects. The V is the void volume, and T is the temperature of the reservoir and sample holder [57]. m is the mass of the sample, and R is the gas constant.

Then, 0.5 g of each sample was transferred to the Sieverts-type reactor without oxygen contact within a sample holder with a closing (isolation) valve. The full testing of materials included calibration, activation, and hydriding/dehydriding cycling. Calibration and operation details were performed as reported elsewhere [57]. In brief, the calibration is performed to determine the void volume (the space not occupied by the sample) in the sample holder by expanding a known aliquot of He gas in isothermal conditions. The activation of the materials was carried out by heating them in a vacuum at 350 °C for 3 h; after that, successive hydriding and dehydriding reactions were performed. For hydriding reactions, hydrogen was allowed in the apparatus at 15 bar. Afterward, the sample was heated from room temperature to 300 °C at a heating rate of 5 °C/min. After finishing the hydriding reaction, the reactor was quickly cooled to room temperature, and the remaining pressure was released. For dehydriding reactions, the hydrogen was initially set in the apparatus at 0.015 bar and then heated to 350 °C at a heating rate of 5 °C/min. After the dehydriding reactions, the complete release of hydrogen from the samples was forced by applying a dynamic vacuum for 30 min at 350 °C. This way, we ensured a completely hydrogen-free material for the following experiment. Then, the samples were cooled to room temperature, and they were ready for the next hydriding/dehydriding cycle. Three and a half cycles were performed in each mixture. The selected threshold to define the beginning of hydriding and dehydriding reactions was ± 0.1 wt. % respectively. XRD and SEM characterization was performed in the materials after hydriding.

Pressure-composition isothermal (PCI) curves were obtained in an Isorb-100 instrument of Quantachrome (Anton Paar GmbH, Ostfildern, Gemany). Samples of about 0.150 g of the as-milled materials were transferred to the instrument without air contact, utilizing a sample holder with an isolation valve. The as-milled materials were heated at 350 °C for 3 h under a dynamic vacuum for activation. The calibration for void volume was performed with ultrahigh-purity helium. Then, the samples were heated to the testing temperature. The experiments were performed at 350 °C, 300 °C, and 250 °C. Once in isothermal conditions, the pressure was gradually increased and decreased in a stepwise manner from 0.01 to 15 bar, and vice versa. PCI curves must be performed in equilibrium conditions, which means long-term experiments. The equilibrium condition was assumed when the recorded pressure presented a variation smaller than 0.1×10^{-3} bar in a time period of 30 min or a maximum duration of 240 min for each step. Reaching the equilibrium directed the change to the subsequent pressure increase or decrease (step). The equilibrium condition criteria directed the total time employed at each experiment, generally between 5 and 7 days per curve. All PCI curves were performed with the same sample, starting with the highest

temperature and progressively reducing the temperature of each experiment. All pressures are reported on an absolute scale, with 0.8 bar as the atmospheric average pressure in the testing location. The hydrogen used during experiments was of chromatographic purity.

4.3. Physicochemical Characterization

All of the as-milled and hydrided materials were characterized with X-ray diffraction (XRD). The powders were compacted into a dedicated sample holder and covered with Kapton (polyimide) tape to protect them from ambient oxygen and moisture. XRD data collection was performed using a D2 Phaser diffractometer from Bruker with a Cu lamp (K_α =1.540598 Å). The XRD data were collected between 10 and 90° in 2θ, with a step of 0.02° and 0.7 seg/step. Crystalline phase identification was performed with the help of the Crystallography Open Database (COD), ICSD FIZ Karlsruhe database, or directly from published data. XRD data was analyzed with MAUD software (version 2.998).

All of the as-milled and hydrided materials were characterized by utilizing scanning electron microscopy (SEM) and elemental mapping. Samples were dispersed on carbon tape and supported in a sample holder inside the argon glove box. Then, the sample holder was confined in a hermetic box filled with argon and moved to the SEM microscope. The samples were briefly exposed to air during insertion into the SEM vacuum chamber. SEM micrographs were collected in a JSM-IT300 microscope with secondary and backscattered electrons at 20 kV of acceleration voltage. Elemental mapping was performed by an SDD X-MaxN EDS detector from Oxford Instruments attached to the microscope.

5. Conclusions

Each added metal, Co, Cu, Fe, and Ni, causes specific effects on the hydriding/dehydriding of the studied materials, $Mg_2(Co_{1/3}Fe_{1/3}Ni_{1/3})$, $Mg_2(Cu_{1/3}Fe_{1/3}Ni_{1/3})$, $Mg_2(Co_{1/3}Cu_{1/3}Fe_{1/3})$, $Mg_2(Co_{1/3}Cu_{1/3}Ni_{1/3})$, and $Mg_2(Co_{1/4}Cu_{1/4}Fe_{1/4}Ni_{1/4})$. Hydriding and dehydriding reactions are primarily two-step processes. The first step corresponds to the Mg/MgH_2 equilibrium. Meanwhile, the second step corresponds to the formation of the mixture of intermetallics and destabilization by $MgCu_2$. The equilibrium pressure of the second step depends on the Cu content. The presence of this metal in the mixture increases the values of the equilibrium pressure of the second step. The combination of Co and Fe enhances hydrogen storage due to the formation of stable Mg-based intermetallics, as observed in Figure 2. Meanwhile, Ni forms the main hydride intermetallic, Mg_2NiH_4. Further research must be carried out to optimize the transition metal content.

Hydriding reactions are easy with low-temperature onset. For improving hydrogen uptake values, hydrogen pressure higher than 15 bar can be used. The lowest dehydriding onset temperature was 243 °C for the $Mg_2(Co_{1/3}Fe_{1/3}Ni_{1/3})$ material. The best-studied material was $Mg_2(Co_{1/3}Fe_{1/3}Ni_{1/3})$ because of the higher hydrogen uptake and lower dehydriding onset temperature.

Supplementary Materials: The following supporting information can be downloaded at: https://www.mdpi.com/article/10.3390/inorganics13050135/s1, Figure S1: Hydriding and dehydriding of $Mg_2(Co_{1/3}Fe_{1/3}Ni_{1/3})$; Figure S2: Detail of XRD of $Mg_2(Co_{1/3}Fe_{1/3}Ni_{1/3})$; Figure S3: SEM of as-milled $Mg_2(Co_{1/3}Fe_{1/3}Ni_{1/3})$; Figure S4: Elemental mapping of as-milled $Mg_2(Co_{1/3}Fe_{1/3}Ni_{1/3})$; Figure S5: SEM of Hydrided $Mg_2(Co_{1/3}Fe_{1/3}Ni_{1/3})$; Figure S6: Elemental mapping of hydrided $Mg_2(Co_{1/3}Fe_{1/3}Ni_{1/3})$; Figure S7: Hydriding and dehydriding of $Mg_2(Cu_{1/3}Fe_{1/3}Ni_{1/3})$; Figure S8: XRD detail of $Mg_2(Cu_{1/3}Fe_{1/3}Ni_{1/3})$; Figure S9: SEM of as-milled $Mg_2(Cu_{1/3}Fe_{1/3}Ni_{1/3})$; Figure S10: Elemental mapping of as-milled $Mg_2(Cu_{1/3}Fe_{1/3}Ni_{1/3})$; Figure S11: SEM of hydrided $Mg_2(Cu_{1/3}Fe_{1/3}Ni_{1/3})$; Figure S12: Elemental mapping of hydrided $Mg_2(Cu_{1/3}Fe_{1/3}Ni_{1/3})$; Figure S13: Hydriding and dehydriding of $Mg_2(Co_{1/3}Cu_{1/3}Fe_{1/3})$; Figure S14: Detail of DRX of $Mg_2(Co_{1/3}Cu_{1/3}Fe_{1/3})$; Figure S15: SEM of as-milled $Mg_2(Co_{1/3}Cu_{1/3}Fe_{1/3})$; Figure S16: Elemental

mapping of as-milled $Mg_2(Co_{1/3}Cu_{1/3}Fe_{1/3})$; Figure S17: SEM of hydrided $Mg_2(Co_{1/3}Cu_{1/3}Fe_{1/3})$; Figure S18: Elemental mapping of hydrided $Mg_2(Co_{1/3}Cu_{1/3}Fe_{1/3})$; Figure S19: Hydriding and dehydriding of $Mg_2(Co_{1/3}Cu_{1/3}Ni_{1/3})$; Figure S20: Detail of DRX of $Mg_2(Co_{1/3}Cu_{1/3}Ni_{1/3})$; Figure S21: SEM of as-milled $Mg_2(Co_{1/3}Cu_{1/3}Ni_{1/3})$; Figure S22: Elemental mapping of as-milled $Mg_2(Co_{1/3}Cu_{1/3}Ni_{1/3})$; Figure S23: SEM of hydrided $Mg_2(Co_{1/3}Cu_{1/3}Ni_{1/3})$; Figure S24: Elemental mapping of hydrided $Mg_2(Co_{1/3}Cu_{1/3}Ni_{1/3})$; Figure S25: Hydriding and dehydriding of $Mg_2(Co_{1/4}Cu_{1/4}Fe_{1/4}Ni_{1/4})$; Figure S26: Detail of DRX of $Mg_2(Co_{1/4}Cu_{1/4}Fe_{1/4}Ni_{1/4})$; Figure S27: SEM of as-milled $Mg_2(Co_{1/4}Cu_{1/4}Fe_{1/4}Ni_{1/4})$; Figure S28: Elemental mapping of as-milled $Mg_2(Co_{1/4}Cu_{1/4}Fe_{1/4}Ni_{1/4})$; Figure S29: SEM of PCT hydrided $Mg_2(Co_{1/4}Cu_{1/4}Fe_{1/4}Ni_{1/4})$; Figure S30: EDS of hydrided $Mg_2(Co_{1/4}Cu_{1/4}Fe_{1/4}Ni_{1/4})$; Figure S31. Maximum dehydriding rate versus temperature. Table S1: Hydrogen storage capacity of $Mg_2(Co_{1/3}Fe_{1/3}Ni_{1/3})$; Table S2: Hydrogen storage capacity of $Mg_2(Cu_{1/3}Fe_{1/3}Ni_{1/3})$; Table S3: Hydrogen storage capacity of $Mg_2(Co_{1/3}Cu_{1/3}Fe_{1/3})$; Table S4: Hydrogen storage capacity of $Mg_2(Co_{1/3}Cu_{1/3}Ni_{1/3})$; Table S5: Hydrogen storage capacity of $Mg_2(Co_{1/4}Cu_{1/4}Fe_{1/4}Ni_{1/4})$.

Author Contributions: Experimentation, E.D.R.-S., P.d.C.C.N. and N.L.T.G.; conceptualization and writing, K.S.-A. All authors have read and agreed to the published version of the manuscript.

Funding: This research was funded by CONAHCYT CF-2023-I-394 Aleaciones de alta entropía con V o Mg para el almacenamiento de hidrógeno. N.L. Torres García (#CVU: 631953) appreciates the support provided by CONAHCYT within Estancias Posdoctorales por Mexico 2024 (3) academic modality.

Data Availability Statement: The original contributions presented in the study are included in the article/Supplementary material, further inquiries can be directed to the corresponding author.

Acknowledgments: Authors acknowledge Orlando Hernández Cristobal for the SEM studies.

Conflicts of Interest: The authors declare no conflicts of interest.

References

1. DOE Technical targets. Available online: https://www.energy.gov/eere/fuelcells/articles/target-explanation-document-onboard-hydrogen-storage-light-duty-fuel-cell (accessed on 9 April 2025).
2. Paul, A.R.; Mehla, S.; Bhargava, S. Intermetallic Compounds for Hydrogen Storage: Current Status and Future Perspectives. *Small* **2024**, *21*, 2408889. [CrossRef] [PubMed]
3. Liu, Y.; Chabane, D.; Elkedim, O. Intermetallic Compounds Synthesized by Mechanical Alloying for Solid-State Hydrogen Storage: A Review. *Energies* **2021**, *14*, 5758. [CrossRef]
4. de Jesús Vega-Soria, J.; Ruiz-Santacruz, E.D.; Torres-García, N.L.; Suárez-Alcántara, K. Systematic study of first-row transition metals chlorides as reaction accelerators for Mg/MgH_2 for hydrogen storage application. *Int. J. Hydrogen Energy* 2024, *in press*. [CrossRef]
5. Bogdanović, B.; Reiser, A.; Schlichte, K.; Spliethoff, B.; Tesche, B. Thermodynamics and dynamics of the Mg–Fe–H system and its potential for thermochemical thermal energy storage. *J. Alloys Compd.* **2002**, *345*, 77–89. [CrossRef]
6. Sai Raman, S.S.; Davidson, D.J.; Bobet, J.L.; Srivastava, O.N. Investigations on the synthesis, structural and microstructural characterizations of Mg-based K_2PtCl_6 type (Mg_2FeH_6) hydrogen storage material prepared by mechanical alloying. *J. Alloys Compd.* **2002**, *333*, 282–290. [CrossRef]
7. Khan, D.; Panda, S.; Ma, Z.; Ding, W.; Zou, J. Formation and hydrogen storage behavior of nanostructured Mg_2FeH_6 in a compressed $2MgH_2$–Fe composite. *Int. J. Hydrogen Energy* **2020**, *45*, 21676–21686. [CrossRef]
8. Chaudhary, A.-L.; Dietzel, S.; Li, H.-W.; Akiba, E.; Bergemann, N.; Pistidda, C.; Klassen, T.; Dornheim, M. Synthesis of Mg_2 FeD_6 under low pressure conditions for Mg_2FeH_6 hydrogen storage studies. *Int. J. Hydrogen Energy* **2017**, *42*, 11422–11428. [CrossRef]
9. Zhang, X.; Yang, R.; Qu, J.; Zhao, W.; Xie, L.; Tian, W.; Li, X. The synthesis and hydrogen storage properties of pure nanostructured Mg_2FeH_6. *Nanotechnology* **2010**, *21*, 095706. [CrossRef]
10. Niaz, N.A.; Ahmad, I.; Khalid, N.R.; Ahmed, E.; Abbas, S.M.; Jabeen, N. Preparation of Mg_2FeH_6 Nanoparticles for Hydrogen Storage Properties. *J. Nanomater.* **2013**, *2013*, 095706. [CrossRef]
11. Leiva, D.R.; Huot, J.; Ishikawa, T.T.; Bolfarini, C.; Kiminami, C.S.; Jorge, A.M.; Botta Filho, W.J. Hydrogen Activation Behavior of Commercial Magnesium Processed by Different Severe Plastic Deformation Routes. *Mater. Sci. Forum* **2010**, *667–669*, 1047–1051. [CrossRef]

12. Didisheim, J.J.; Zolliker, P.; Yvon, K.; Fischer, P.; Schefer, J.; Gubelmann, M.; Williams, A.F. Dimagnesium iron(II) hydride, Mg_2FeH_6, containing octahedral FeH_6^{4-} anions. *Inorg. Chem.* **1984**, *23*, 1953–1957. [CrossRef]
13. Bashir, A.I.; Arif, H.; Azam, S.; Irfan, M.; Khan, N. First-principles quantum computations to investigate prospects of Mg_2FeH_6 for optoelectronics and hydrogen-storage applications. *Int. J. Hydrogen Energy* **2023**, *48*, 23930–23942. [CrossRef]
14. Zhang, J.; Cuevas, F.; Zaïdi, W.; Bonnet, J.-P.; Aymard, L.; Bobet, J.-L.; Latroche, M. Highlighting of a Single Reaction Path during Reactive Ball Milling of Mg and TM by Quantitative H_2 Gas Sorption Analysis to Form Ternary Complex Hydrides (TM = Fe, Co, Ni). *J. Phys. Chem. C* **2011**, *115*, 4971–4979. [CrossRef]
15. Zolliker, P.; Yvon, K.; Fischer, P.; Schefer, J. Dimagnesium cobalt(I) pentahydride, Mg_2CoH_5, containing square-pyramidal pentahydrocobaltate(4-) (CoH_5^{4-}) anions. *Inorg. Chem.* **1985**, *24*, 4177–4180. [CrossRef]
16. Norek, M.; Nielsen, T.K.; Polanski, M.; Kunce, I.; Płociński, T.; Jaroszewicz, L.R.; Cerenius, Y.; Jensen, T.R.; Bystrzycki, J. Synthesis and decomposition mechanisms of ternary Mg_2CoH_5 studied using in situ synchrotron X-ray diffraction. *Int. J. Hydrogen Energy* **2011**, *36*, 10760–10770. [CrossRef]
17. Černý, R.; Bonhomme, F.; Yvon, K.; Fischer, P.; Zolliker, P.; Cox, D.E.; Hewat, A. Hexamagnesium dicobalt undecadeuteride Mg6Co2D11: Containing $[CoD_4]^{5-}$ and $[CoD_5]^{4-}$ complex anions conforming to the 18-electron rule. *J. Alloys Compd.* **1992**, *187*, 233–241. [CrossRef]
18. Nayeb-Hashemi, A.A.; Clark, J.B. The Co-Mg (Cobalt-Magnesium) system. *Bull. Alloy Phase Diagrams* **1987**, *8*, 352–355. [CrossRef]
19. Matheus, F.H.; Zepon, G.; Oliveira, V.B.; Leiva, D.R. Highly reactive hydrogen storage Mg_2Ni alloy prepared by mechanochemistry and H-cycling. *Int. J. Hydrogen Energy* **2023**, *51*, 320–328. [CrossRef]
20. Lyu, J.; Lider, A.; Kudiiarov, V. Using Ball Milling for Modification of the Hydrogenation/Dehydrogenation Process in Magnesium-Based Hydrogen Storage Materials: An Overview. *Metals* **2019**, *9*, 768. [CrossRef]
21. Janot, R.; Aymard, L.; Rougier, A.; Nazri, G.A.; Tarascon, J.M. Fast hydrogen sorption kinetics for ball-milled Mg_2Ni alloys. *J. Phys. Chem. Solids* **2004**, *65*, 529–534. [CrossRef]
22. Ebrahimi-Purkani, A.; Kashani-Bozorg, S.F. Nanocrystalline Mg_2Ni-based powders produced by high-energy ball milling and subsequent annealing. *J. Alloys Compd.* **2008**, *456*, 211–215. [CrossRef]
23. Baraban, A.P.; Dmitriev, V.A.; Gabis, I.E.; Voyt, A.P.; Klyamkin, S.N.; Shikin, I.V. Direct synthesis of Mg_2NiH_4 from MgH_2 and Ni. *Phys. Complex Syst.* **2023**, *4*, 94–102. [CrossRef]
24. Zolliker, P.; Yvon, K.; Jorgensen, J.D.; Rotella, F.J. Structural studies of the hydrogen storage material magnesium nickel hydride (Mg_2NiH_4). 2. Monoclinic low-temperature structure. *Inorg. Chem.* **1986**, *25*, 3590–3593. [CrossRef]
25. Vajo, J.J.; Mertens, F.; Ahn, C.C.; Bowman, R.C.; Fultz, B. Altering hydrogen storage properties by hydride destabilization through alloy formation: LiH and MgH_2 destabilized with Si. *J. Phys. Chem. B* **2004**, *108*, 13977–13983. [CrossRef]
26. Reilly, J.J.; Wiswall, R.H. Reaction of hydrogen with alloys of magnesium and copper. *Inorg. Chem.* **1967**, *6*, 2220–2223. [CrossRef]
27. Andreasen, A.; Sørensen, M.B.; Burkarl, R.; Møller, B.; Molenbroek, A.M.; Pedersen, A.S.; Vegge, T.; Jensen, T.R. Dehydrogenation kinetics of air-exposed MgH_2/Mg_2Cu and $MgH_2/MgCu_2$ studied with in situ X-ray powder diffraction. *Appl. Phys. A Mater. Sci. Process.* **2006**, *82*, 515–521. [CrossRef]
28. Dai, J.; Jiang, B.; Zhang, J.; Yang, Q.; Jiang, Z.; Dong, H.; Pan, F. Diffusion Kinetics in Mg-Cu Binary System. *J. Phase Equilibria Diffus.* **2015**, *36*, 613–619. [CrossRef]
29. Jurczyk, M.; Okonska, I.; Iwasieczko, W.; Jankowska, E.; Drulis, H. Thermodynamic and electrochemical properties of nanocrystalline Mg_2Cu-type hydrogen storage materials. *J. Alloys Compd.* **2007**, *429*, 316–320. [CrossRef]
30. Li, J.; Liu, L.; Cui, M. Study on the synthesis and hydrogen storage properties of Mg_2CuH_3. *Int. J. Hydrogen Energy* **2016**, *41*, 13152–13155. [CrossRef]
31. Verbovytskyy, Y.; Zhang, J.; Cuevas, F.; Paul-Boncour, V.; Zavaliy, I. Synthesis and properties of the $Mg_2Ni_{0.5}Co_{0.5}H_{4.4}$ hydride. *J. Alloys Compd.* **2015**, *645*, S408–S411. [CrossRef]
32. Chen, Y.; Huang, H.; Fu, J.; Guo, Q.; Pan, F.; Deng, S.; Li, J.; Zhao, G. The synthesis and hydrogen storage properties of Mg_2Ni substituted with Cu, Co. *J. Mater. Res.* **2009**, *24*, 1311–1316. [CrossRef]
33. Saita, I.; Saito, K.; Akiyama, T. Hydriding combustion synthesis of $Mg_2Ni_{1-x}Fe_x$ hydride. *J. Alloys Compd.* **2005**, *390*, 265–269. [CrossRef]
34. Mendoza-Zélis, L.; Meyer, M.; Baum, L. Complex quaternary hydrides Mg_2(Fe,Co)Hy for hydrogen storage. *Int. J. Hydrogen Energy* **2011**, *36*, 600–605. [CrossRef]
35. Polanski, M.; Płociński, T.; Kunce, I.; Bystrzycki, J. Dynamic synthesis of ternary Mg_2FeH_6. *Int. J. Hydrogen Energy* **2010**, *35*, 1257–1266. [CrossRef]
36. Fernández, I.G.; Meyer, G.O.; Gennari, F.C. Hydriding/dehydriding behavior of Mg_2CoH_5 produced by reactive mechanical milling. *J. Alloys Compd.* **2008**, *464*, 111–117. [CrossRef]
37. Chen, J.; Takeshita, H.T.; Chartouni, D.; Kuriyama, N.; Sakai, T. Synthesis and characterization of nanocrystaline Mg_2CoH_5 obtained by mechanical alloying. *J. Mater. Sci.* **2001**, *36*, 5829–5834. [CrossRef]

38. Fernández, I.G.; Meyer, G.O.; Gennari, F.C. Reversible hydrogen storage in Mg_2CoH_5 prepared by a combined milling-sintering procedure. *J. Alloys Compd.* **2007**, *446–447*, 106–109. [CrossRef]
39. Lu, X.; Zhang, L.; Zheng, J.; Yu, X. Construction of carbon covered Mg_2NiH_4 nanocrystalline for hydrogen storage. *J. Alloys Compd.* **2022**, *905*, 164169. [CrossRef]
40. Shao, H.; Xu, H.; Wang, Y.; Li, X. Preparation and hydrogen storage properties of Mg_2Ni intermetallic nanoparticles. *Nanotechnology* **2004**, *15*, 269–274. [CrossRef]
41. Hsu, F.-K.; Hsu, C.-W.; Chang, J.-K.; Lin, C.-K.; Lee, S.-L.; Jiang, C.-E. Structure and hydrogen storage properties of $Mg_2Cu_{1-x}Ni_x$ (x=0–1) alloys. *Int. J. Hydrogen Energy* **2010**, *35*, 13247–13254. [CrossRef]
42. Darnaudery, J.; Darriet, B.; Pezat, M. The $Mg_2Ni_{0.75}M_{0.25}$ alloys (M = 3d element): Their application to hydrogen storage. *Int. J. Hydrogen Energy* **1983**, *8*, 705–708. [CrossRef]
43. Deledda, S.; Hauback, B.C. The formation mechanism and structural characterization of the mixed transition-metal complex hydride Mg_2 $(FeH_6)_{0.5}(CoH_5)_{0.5}$ obtained by reactive milling. *Nanotechnology* **2009**, *20*, 204010. [CrossRef] [PubMed]
44. Züttel, A. Materials for hydrogen storage. *Mater. Today* **2003**, *6*, 24–33. [CrossRef]
45. Webbook NIST. Available online: https://webbook.nist.gov/chemistry/ (accessed on 9 April 2025).
46. Reilly, J.J.; Wiswall, R.H. Reaction of hydrogen with alloys of magnesium and nickel and the formation of Mg_2NiH_4. *Inorg. Chem.* **1968**, *7*, 2254–2256. [CrossRef]
47. Zareii, S.M.; Sarhaddi, R. Structural, electronic properties and heat of formation of Mg_2FeH_6 complex hydride: An ab initio study. *Phys. Scr.* **2012**, *86*, 015701. [CrossRef]
48. Zhou, S.; Wang, Y.; Shi, F.G.; Sommer, F.; Chen, L.-Q.; Liu, Z.-K.; Napolitano, R.E. Modeling of Thermodynamic Properties and Phase Equilibria for the Cu-Mg Binary System. *J. Phase Equilibria Diffus.* **2007**, *28*, 158–166. [CrossRef]
49. Mezbahul-Islam, M.; Mostafa, A.O.; Medraj, M. Essential Magnesium Alloys Binary Phase Diagrams and Their Thermochemical Data. *J. Mater.* **2014**, *2014*, 704283. [CrossRef]
50. Babenko, A.; Ghasali, E.; Raza, S.; Baghchesaraee, K.; Cheng, Y.; Hayat, A.; Liu, P.; Zhao, S.; Orooji, Y. Comprehensive insights into recent innovations: Magnesium-inclusive high-entropy alloys. *J. Magnes. Alloy.* **2024**, *12*, 1311–1345. [CrossRef]
51. Ruiz-Santacruz, E.D.; Vega-Soria, J.d.J.; Cruz-Jiménez, A.K.; Caudillo-Flores, U.; Torres-García, N.L.; Suárez-Alcántara, K. High-load Mg_2Ni nanoparticle-carbon nanofiber composites for hydrogen storage. *Nanoscale* **2024**, *16*, 17908–17925. [CrossRef]
52. Baum, L.; Meyer, M.; Mendozazelis, L. Complex Mg-based hydrides obtained by mechanosynthesis: Characterization and formation kinetics. *Int. J. Hydrogen Energy* **2008**, *33*, 3442–3446. [CrossRef]
53. Wang, L.; Zhang, L.; Lu, X.; Wu, F.; Sun, X.; Zhao, H.; Li, Q. Surprising cocktail effect in high entropy alloys on catalyzing magnesium hydride for solid-state hydrogen storage. *Chem. Eng. J.* **2023**, *465*, 142766. [CrossRef]
54. Wan, H.; Yang, X.; Zhou, S.; Ran, L.; Lu, Y.; Chen, Y.; Wang, J.; Pan, F. Enhancing hydrogen storage properties of MgH_2 using FeCoNiCrMn high entropy alloy catalysts. *J. Mater. Sci. Technol.* **2023**, *149*, 88–98. [CrossRef]
55. Gupta, A.; Faisal, M.; Flamina, A.; Raghavendra, R.M.; Hassan, F.; Kundan, N.; Kumar, N. Enhanced hydrogen storage in Mg catalysed by Cu–Ni–Co–Fe quaternary multi-component alloy. *Int. J. Hydrogen Energy* **2024**, *50*, 932–945. [CrossRef]
56. Zhang, C.; Yang, Y. The CALPHAD approach for HEAs: Challenges and opportunities. *MRS Bull.* **2022**, *47*, 158–167. [CrossRef]
57. Carrillo-Bucio, J.L.; Tena-Garcia, J.R.; Armenta-Garcia, E.P.; Hernandez-Silva, O.; Cabañas-Moreno, J.G.; Suárez-Alcántara, K. Low-cost Sieverts-type apparatus for the study of hydriding/dehydriding reactions. *HardwareX* **2018**, *4*, e00036. [CrossRef]

Disclaimer/Publisher's Note: The statements, opinions and data contained in all publications are solely those of the individual author(s) and contributor(s) and not of MDPI and/or the editor(s). MDPI and/or the editor(s) disclaim responsibility for any injury to people or property resulting from any ideas, methods, instructions or products referred to in the content.